Continuous hydrophoretic separation and sizing of microparticles using slanted obstacles in a microchannel†‡

Sungyoung Choi and Je-Kyun Park*

We report a microfluidic separation and sizing method of microparticles with hydrophoresis—the movement of suspended particles under the influence of a microstructure-induced pressure field. By exploiting slanted obstacles in a microchannel, we can generate a lateral pressure gradient so that microparticles can be deflected and arranged along the lateral flows induced by the gradient. Using such movements of particles, we completely separated polystyrene microbeads with 9 and 12 μm diameters. Also, we discriminated polystyrene microbeads with diameter differences of ~7.3%. Additionally, we measured the diameter of 10.4 μm beads with high coefficient of variation and compared the result with a conventional laser diffraction method. The slanted obstacle as a microfluidic control element in a microchannel is analogous to the electric, magnetic, optical, or acoustic counterparts in that their function is to generate a field gradient. Since our method is based on intrinsic pressure fields, we could eliminate the need for external potential fields to induce the movement of particles. Therefore, our hydrophoretic method will offer a new opportunity for power-free and biocompatible particle control within integrated microfluidic devices.

Introduction

Size-based separation is widely used in biotechnology, from blood cell separation to multianalyte and flow-assisted immunoassays.[1–3] For these purposes, conventional flow-assisted separation techniques and their microfabricated counterparts have been developed, such as field flow fractionation (FFF) and split-flow thin fractionation (SF).[4–12] Among the various FFF methods, sedimentation FFF (SdFFF), gravitational FFF (GrFFF), and their combination method with dielectrophoresis (DEP-FFF) were mainly used for applications of micron-sized particles, providing biocompatible and sterilized protocols.[5–10] However, particle separation in GrFFF and DEP-FFF is not conducted in a continuous manner, which gives some disadvantages of both restricted amounts of samples within separation chamber volumes and relatively long separation times.[7–10] SF, one of the continuous fractionation methods, was applied to separation of human blood cells using centrifugal and magnetic fields.[11,12] These active separation approaches using external potential fields have some drawbacks. For example, a native complexity arises from the integration of rotation stages.

Separation technologies in a microfluidic environment can bring several more advantages over macroscale systems. These advantages include more accurate particle control without

turbulent disturbance due to laminar flow at low Reynolds number (Re) and higher process efficiency even with small numbers of particles.[13,14] Recently, several size-based separation methods have demonstrated their effectiveness in microfluidics utilizing dielectrophoresis (DEP), magnetophoresis (MP), optical fields, and flow-assisted methods.[15–25] Compared with flow-assisted methods, active separation techniques using DEP and MP require relatively complex fabrication processes such as patterning of metal-electrodes and magnetic structures.[15–18] Also, DEP is often limited in biological applications because of buffer incompatibility.[19] Optical methods depend on the accurate beam alignment between separation targets and complex optical instruments.[20,21] Because flow-assisted methods utilize inherent hydrodynamic phenomena, they can disregard above-mentioned problems. However, their dependence on laminar streams makes it difficult to induce the dynamic movement of particles from one sidewall of a channel to the other sidewall along field gradients as in the active methods. Therefore, it is necessary for particle separation to confine particles in a certain position of a fluid stream with sheath flows,[22,23] or to divide and re-distribute fluid streams with complex channel networks.[24,25] In particular, the former techniques based on sheath flows require an accurate flow control between the sample and sheath flows. The imperfect confinement of particles by unstable pumping defocuses their initial position and results in a decrease of separation efficiency.

Here, we present continuous hydrophoretic separation of microparticles using slanted obstacles and its application to particle sizing. We have previously developed a novel separation system using the horizontal deflection of particles around slanted obstacles.[26] In this study, we first introduce the concept of "hydrophoresis" to explain the ordered particle

Department of BioSystems, Korea Advanced Institute of Science and Technology (KAIST), 373-1 Guseong-dong, Yuseong-gu, Daejeon, 305-701, Republic of Korea. E-mail: jekyun@kaist.ac.kr; Fax: +82 42 869 4310; Tel: +82 42 869 4315
† The HTML version of this article has been enhanced with colour images.
‡ Electronic supplementary information (ESI) available: Supplementary video in mpg format. See DOI: 10.1039/b701227f

movement. Hydrophoresis means the movement of suspended particles under the influence of a microstructure-induced pressure field. Our hydrophoretic separation method utilizes slanted obstacles to create transverse flows perpendicular to the direction of a fluid flow for the manipulation of particles. The transverse flows result from an anisotropic fluidic resistance of the slanted obstacle. The top- or bottom-area of the slanted obstacles has higher resistance than the side area of the obstacles. Particles subjected to the lateral pressure gradients or flows induced by the anisotropy dynamically move from the one sidewall of a channel to the other sidewall without any active component. The hydrophoretic separation method exhibits both advantages of the active and passive methods which are dynamic particle manipulation and biocompatibility, respectively. Moreover, hydrophoresis based on intrinsic pressure fields enables a flow-rate independent separation—difficult to achieve in the active methods that are usually under the influence of flow rate. This study deals with the hydrophoretic movement of particles by their sizes. The transverse position of particles depends on the particle size and is insensitive to the flow rate. The behavior of separated particles is explained in detail with the pressure field simulation by computational fluid dynamics (CFD) software. We also demonstrated the continuous separation of 9 and 12 μm beads. The separation profile is linearly changed according to the particle size. We utilized these size-dependent hydrophoretic movements of particles as the signal for particle sizing. The size measurement of 10.4 μm beads with high coefficient of variation was demonstrated and compared with a conventional laser diffraction method.

Separation principle

Fig. 1 illustrates overall focusing and separation processes of the small and large particles passing the slanted obstacles with their schematic trajectories and schematic velocity vectors. The slanted obstacles are formed on the bottom and top of a channel. Its height is defined as half of the channel height. The anisotropy of a fluidic resistance between the top- or bottom-area and side-area of the obstacles generates lateral pressure gradients, which induce helical recirculation.[26,27] The directions of the recirculation are clockwise and counter-clockwise for lower and upper obstacles, respectively. The clockwise recirculation induced by the lower obstacle has a sequence of a deviation, upward, focusing, downward, and deviation flows (1–3 in Fig. 1c). The counter-clockwise recirculation induced by the upper obstacle has a sequence of a deviation, downward, focusing, upward, and deviation flows (4–6 in Fig. 1c).

When particles pass through the slanted obstacles alternately placed on the bottom and top of a channel, they are focused to a sidewall in the direction of the focusing flow. The second region is designed with the slanted obstacles only at the bottom of the channel (Fig. 1b). The sequential obstacles at the bottom generate rotating flows only in a clockwise direction. Following the downward flows of the rotating flows, the particles take their positions at the bottom of the channel. In the third region, the deviation degree of the particles from the focused position depends on the relative size-differences of the particles to the gap between the slanted obstacles and the top or bottom of the channel (Fig. 1c). The large particle which has a comparable size to the gap of the obstacles is aligned at the center of z-axis by the obstacles. In that region, the deviation flow is absent in the rotating flows, which keeps the particle in its focused position. The large particle is just moving up and down following the upward and downward flows (see the arrows of the large particle in 3 and 6 of Fig. 1c). We call this motion the "direct mode." In contrast, the small particle at the bottom of a channel is exposed to lateral pressure gradients along the x-axis of the rotating flows. It oscillates following the focusing and deviation flows (see the arrows of the small particle in 1–6 of Fig. 1c). Without the z-axis positioning in the second region, the small particle can be at the center of z-axis and move like the large particle in the direct mode. The small particle deviates from its focused position in
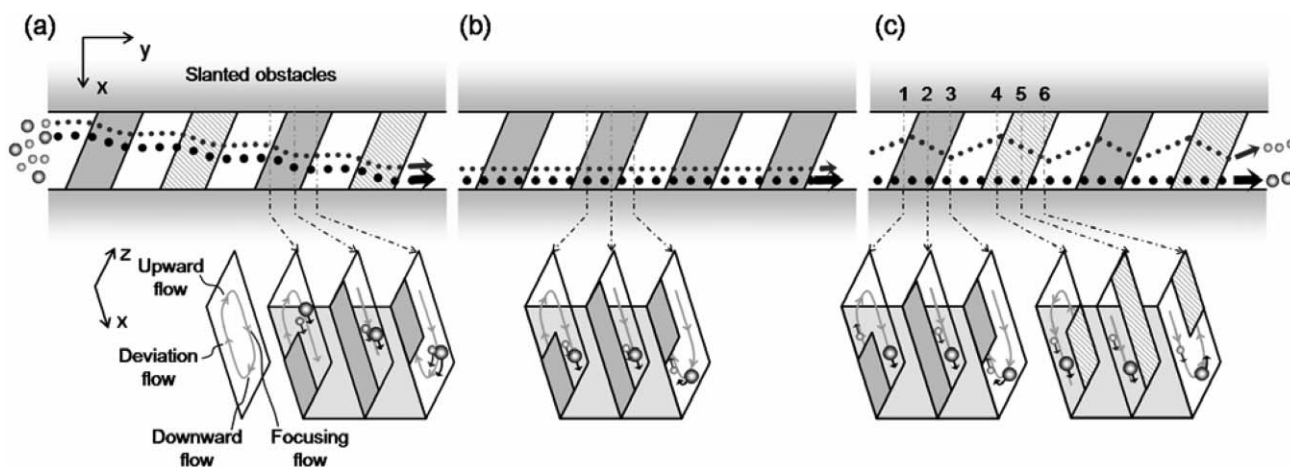

Fig. 1 Hydrophoretic separation principle. Shaded- and lined-areas denote lower and upper slanted obstacles, respectively. A flow direction is along the y-axis. (a–c) Top-viewing and cross-sectional schematic diagrams of the slanted obstacles. (a) The slanted obstacles drive lateral flows across the x-axis by which particles are pushed to a sidewall. (b) The focused particles flow clockwise following the rotating flows generated by the bottom-side obstacles and move to the bottom of a channel. (c) The large particle is located in the area where there is no lateral pressure gradients and stays in the focused position. On the other hand, the small particle is exposed to lateral pressure gradients along the x-axis and deviates from its focused position.

the side areas of the slanted obstacles (1 and 3 of Fig. 1c). Other times, it returns to the focused position in the top- and bottom-area of the obstacles (2, 4, and 5 of Fig. 1c). This oscillation makes the small particle deviate from its previously focused position. We refer this separation motion as the "oscillating mode." Through these hydrophoretic procedures, we can separate microparticles by size without any external potential field and complex channel networks.

Experimental

Design and fabrication of microfluidic device

The microfluidic device for hydrophoretic separation and sizing is a stacked structure of two poly(dimethylsiloxane) (PDMS)-channel layers with upper and lower obstacles (Fig. 2). The channel of the microfluidic device is consisted of a series of slanted obstacles. The first region has 18 slanted obstacles alternately formed on the top and bottom of the channel (1 of Fig. 2). The second region has 8 slanted obstacles formed only on the bottom (2 of Fig. 2). The third region has 12 slanted obstacles alternately formed on the top and bottom of the channel (3 of Fig. 2). The fourth region has 15 slanted obstacles alternately formed on the top and bottom of the channel (4 of Fig. 2). In these structures, the first region is for the focusing process to a sidewall (Fig. 1a), the second region is for the alignment process to the bottom (Fig. 1b), and the third and fourth regions are for the separation process (Fig. 1c). The slanted obstacles in the first to third regions were designed with smaller geometric parameters than the slanted obstacles for the fourth region to reduce the length of the channel. The slanted obstacles in (1) to (3) of Fig. 2 were defined with $W = 50$ μm, $Q = 35$ μm, $S = 105$ μm, and $\theta = 55°$. The slanted obstacles in (4) of Fig. 2 were defined with $W = 100$ μm, $Q = 70$ μm, $S = 210$ μm, and $\theta = 55°$. The whole channel was ~10 mm in length.

The microfluidic device for hydrophoretic separation and sizing was fabricated in PDMS using a soft lithography process. The mixture of PDMS prepolymer and curing agent (Sylgard 184; Dow Corning, MI) in the ratio of 5 : 1 was poured on the photoresist (PR) mold and cured for ~3 h in a convection oven of 65 °C. To align and bond between the PDMS replicas (one with upper obstacles and the other with lower obstacles), after their brief treatment with oxygen plasma (200 mTorr, 200 W), we dipped them into ethyl alcohol solution. Since the oxidized surfaces of PDMS are preserved under liquid solutions, we could align and bond them together. Accordingly, the height of the obstacles (H_{so}) was defined as the half of the channel height (H_{ch}). The exact heights of slanted obstacles with 19, 23, and 25 μm nominal heights were 19.22 ± 0.08, 23.02 ± 0.22, and 25.04 ± 0.26 μm.

Preparation of polystyrene microspheres

Plain polystyrene beads of 8, 9, 10, 11, 12, 15, and 20 μm nominal diameter (Sigma–Aldrich Co., MO, USA) were used for the demonstration of hydrophoretic separation and sizing. The beads were prepared in 0.2% Tween®20 aqueous buffer with concentrations of ~380, 260, 240, 250, 150, 158, and 165 μL^{-1} for 8 to 20 μm beads, respectively. Their exact diameters were 8.02, 9.26, 10.09, 10.98, 11.85, 14.78, and 19.75 μm, respectively. They had coefficient of variation (CV) less than 2% for particle size. Polystyrene beads with 10.4 μm diameter and relatively high CV of 8.7% (Polysciences, Inc., PA, USA) were also used for the demonstration of hydrophoretic sizing. 10.4 μm beads were prepared at a concentration of 238 μL^{-1}.

Experimental setup

Bead mixtures were introduced into the microfluidic device using a syringe pump (Pump 11 Pico Plus; Harvard Apparatus, Inc., MA, USA). Particle images and videos were taken with a CCD camera (DS-2MBWc; Nikon Co., Japan) equipped with an inverted optical microscope (TS100; Nikon Co., Japan). The lateral position of particles was measured from captured images in the expanded outlet region with 1 mm width. A commercial image analyzing program, i-Solution (iMTechnology Co., Korea) was used to measure the position of particles. This program determines the particle position by the calibrated pixel information. The images to measure the particle position were acquired in the resolution of 1024 × 768 pixels. In each experiment, more than 100 particles were measured. Microparticle separation experiments were repeated four times. For particle sizing, 1071 particles with 10.4 μm diameter were measured. The pressure distributions and gradients in a microchannel were simulated using a commercial CFD solver (CFD-ACE+; CFD Research Co., Huntsville, AL, USA).
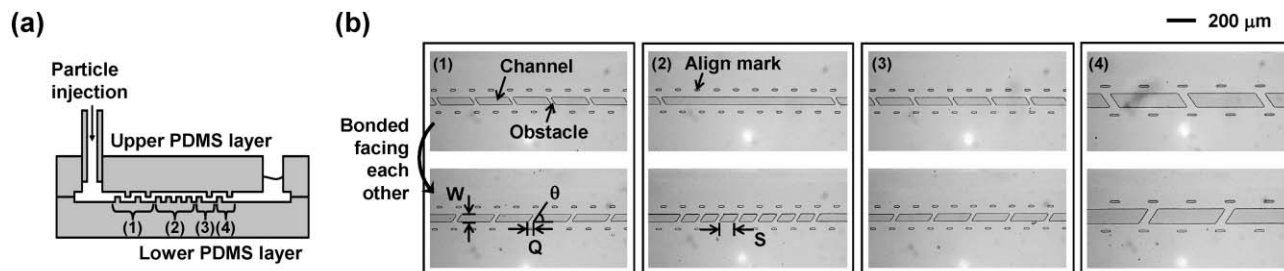

Fig. 2 Microfluidic device for hydrophoretic separation. (a) Cross-sectional schematic diagram of the device after bonding. (b) Optical micrographs showing slanted obstacles before bonding. A PDMS layer (b, upper) with upper slanted obstacles was bonded to the other PDMS layer (b, lower) with lower slanted obstacles facing each other. The upper region of (2) in (b) has no slanted obstacles to form slanted obstacles only at the bottom of a channel. In this section, particles were arranged to the bottom of the channel. In other sections, slanted obstacles were alternately formed on the bottom and top of the channel.

Results and discussion

Size-dependent movements of particles passing slanted obstacles

Using the device with 19 μm-height slanted obstacles, we observed that particles passing them show two separation modes. In this test, we used microspheres with diameters of 9 and 12 μm. The applied flow rate was 0.1 μL min^{-1}. Fig. 3 shows the trajectories of 9 and 12 μm microspheres in the fourth channel region (4 of Fig. 2). The time interval between particles in each image was 1/15 s. Regardless of their initial positions, the microspheres were focused to the lower sidewall of the channel. Also, the deflection of the particles to the sidewall occurred right at the top- and bottom-area of the slanted obstacles. This is because transverse flows are mainly localized on the top- and bottom-area of the obstacles, not their front- or rear-area (2 and 5 of Fig. 1c). In the front and rear of the slanted obstacles, the particle movements follow rotating flows in a clockwise or counterclockwise direction (1 and 3 of Fig. 1c). As a result of hydrophoretic procedures, the 9 μm bead flowed in the oscillating mode around the center of the channel (the upper of Fig. 3). In contrast, the 12 μm bead stayed in its focused position by the alignment effect (the lower of Fig. 3).

The alternate placement of slanted obstacles on the bottom and top of a channel plays an important role in hydrophoretic separation. The obstacles on the bottom of a channel generate rotating flows in a clockwise direction. When we placed slanted obstacles only at the bottom of a channel, the particle movement by the clockwise rotation flows was in disorder (data not shown). The clockwise rotation flows include not only focusing-flows along the x-axis (the upper channel area above the obstacle), but also deviation-flows from the focusing region (the lower channel area beneath the obstacle) as shown in Fig. 1b. Therefore, particles in the upper channel area deflect to the focusing region. After complete focusing, the particles move from the upper channel area to the lower area following the downward flows. Then, they deviate from their focused position meeting the deviation-flows. Repeating these procedures, particles travel back and forth between one sidewall and the other sidewall. However, the obstacles alternately formed on the bottom and top of a channel generate rotating flows in a clockwise and counterclockwise
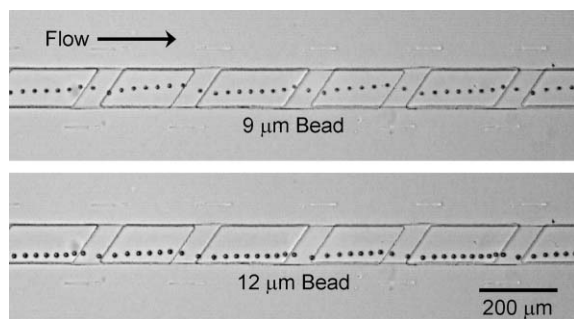
direction. This alternate rotating flow prevents the deviation of focused particles in the direct mode.

Simulation of pressure fields around slanted obstacles

Fig. 4a shows the computed contour of the pressure magnitude in each cross-section of a microchannel with a lower and upper slanted obstacle. The insets are the enlarged views of the projected velocity vectors around the lower slanted obstacle. The geometric conditions are identical with the experimental ones in Fig. 3. The applied flow rate was 0.1 μL min^{-1} along the y-axis. The simulated pressure fields were normalized for the clear illustration in each cross-section. Also, we plotted the calculated pressure gradients along the line from A to B in Fig. 4a to investigate the influence of the flow rate on the pressure gradient (Fig. 4b).

As shown in Fig. 4a, the pressure field varies significantly around slanted obstacles. The pressure field is maximum near the left sidewall and the smallest field appears near the right sidewall. This anisotropy of the pressure strength drives the

Fig. 3 Optical micrographs showing trajectories of 9 and 12 μm beads passing 19 μm-height slanted obstacles at 0.1 μL min^{-1}. While the 9 μm bead was deviated from the focused position (the lower side of the channel), the 12 μm bead stayed in the focused position.
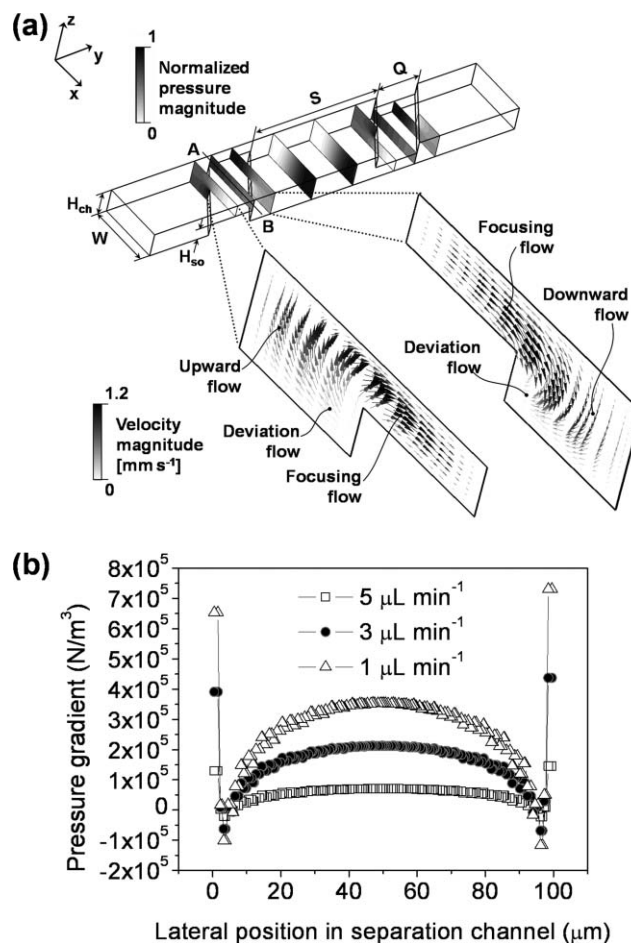

Fig. 4 Simulated pressure fields. (a) The simulation geometry composed of lower and upper slanted obstacles and the cross-sectional plots of pressure distributions at the applied flow rate of 0.1 μL min^{-1} along the y-axis. The enlarged plots describe the projected velocity vectors to the cross-sectional surfaces. (b) Plot of calculated pressure gradients along the line from A to B in (a). The magnitude of the pressure gradient increases by the flow rate.

helical recirculation consisted of upward, focusing, downward, and deviation flows (see the insets of Fig. 4a). The pressure fields around the slanted obstacles generate lateral flows along the x-axis, which in turn induce the particle focusing movement. The direction of the pressure magnitude is inversed in the channel region between the lower and upper obstacle. In that region, the direction of the pressure field is from the right sidewall to the left sidewall. This inversed field direction explains why the particles deviated from their focusing positions in the channel region between obstacles (Fig. 3). The separated movement of particles with different sizes is attributed to the different positions along the z-axis. When the large particle, which has a comparable size to the obstacle, is focused to the right sidewall, it can be aligned at the center of the z-axis passing the obstacle. In that region, the pressure gradient and velocity vectors are formed in the direction of the z-axis, not the x-axis. Therefore, the large particle can stay in its focused position moving up and down. On the other hand, the small particle at the bottom of a channel is exposed to the lateral pressure gradient, and thus deviates from its focused position. Fig. 4b shows the computed pressure gradients at three different flow rates of 1, 3, and 5 μL min^{-1}. The maximum intensity of the pressure gradient increases in proportion to the flow rate. The pressure gradient at 5 μL min^{-1} is ~5 times as high as that at 1 μL min^{-1}. Therefore, even at higher flow rates, particles are exposed to increased lateral pressure gradients and move rapidly. The overall effects are independent of the flow rate.

Effect of the particle diameter on hydrophoretic separation

The lateral position of particles is a function of the size of a particle relative to the gap of slanted obstacles. Using devices with 19 μm-height slanted obstacles, size-standard microspheres with diameters of 8 to 12 μm were individually characterized into specific lateral positions at a flow rate of 1 μL min^{-1} (Fig. 5a). As we increased the flow rate from 0.1 to 1.0 μL min^{-1}, the 9 and 12 μm beads still kept their separation modes in the device with 19 μm-height slanted obstacles. The lateral positions of all particles were discriminated and had coefficients of variance (CVs) of 7.2, 4.0, 3.6, 2.8, and 0.7% for 8, 9, 10, 11, and 12 μm particles, respectively. The CVs of the lateral position were calculated by the following equation.[22]

$$CV_{LP} = \frac{\left|\frac{dD}{dx}\right| \Delta x}{\langle D \rangle} \times 100(\%) \qquad (1)$$

where CV_{LP} is the CV of the lateral position, x is the lateral position from the right sidewall, Δx is the standard deviation of the lateral position, D is the particle diameter, and $\langle D \rangle$ is the mean of the particle diameter. The CVs of the lateral positions for 11 and 12 μm particles show similar values to the ~2% CV for their sizes. This uncertainty of the lateral positions of the particles in the direct mode is attributed to the inhomogeneity of their sizes. In contrast, 8 to 10 μm particles have higher CVs than the ~2% CVs for their sizes. We can presume that this phenomenon results from different distribution ranges on the z-axis by size. In the separation procedure, large particles, which have a comparable size to the gap of
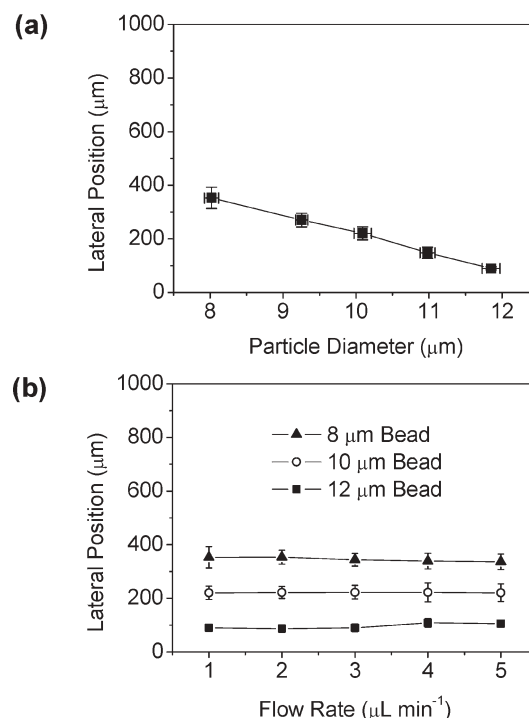

Fig. 5 (a) The linear characteristic of "lateral position *versus* particle diameter." The flow rate of 1 μL min^{-1} was applied to the microfluidic devices with obstacle heights of 19 μm. Particles were measured in the expanded outlet region of 1 mm. (b) Measured particle positions at varying flow rates from 1 to 5 μL min^{-1} in the devices with 19 μm-height obstacles. Each error bar represents the standard deviation from the measurement of more than 100 particles.

slanted obstacles, can be located in relatively narrow ranges on the z-axis by the alignment effect. They are exposed to a common pressure field, thereby being separated in more uniform lateral positions. On the other hand, smaller particles can be located in wider ranges on the z-axis and exposed to different pressure fields according to their positions on the z-axis. Therefore, the CV for the lateral position increases as the size of the particle decreases.

Effect of the flow rate on hydrophoretic separation

Fig. 5b shows the independence of the particle position on the flow rate in the microfluidic device with 19 μm-height obstacles. Size-standard microspheres with diameters of 8, 10, and 12 μm were individually characterized as the flow rate was changed from 1 to 5 μL min^{-1}. As shown in Fig. 5b, the particle position was not affected by the increase of the flow rate. The higher flow rate increases the pressure drop between the front and rear of slanted obstacles, resulting in the increase of the lateral pressure gradient. Although particles pass slanted obstacles faster, they can be exposed to higher transverse flows and deflect faster. Therefore, the particles stayed in the same position regardless of the flow rate.

In hydrophoretic separation, the influence of gravity should be pointed out because the polystyrene particles with a density of 1.05 g cm^{-3} will settle under the gravitational force of the earth. Ignoring the presence of slanted obstacles in a channel, the linear velocity of particles passing the separation channel

at a flow rate of 5 µL min^{-1} is ~4.4 and 2.2 cm s^{-1} in channel widths of 50 and 100 µm, respectively. From the experimental results, the particles can separate within 0.32 s. By Stokes' law, a 12 µm bead in water at 20 °C has a settling velocity of ~4 µm s^{-1} and a settling distance of 1.3 µm in the separation channel. In our experiments, the gravitational settling is negligible due to the relatively short settling distance compared to the channel height of 38 µm. The corresponding height of slanted obstacles is 19 µm. Also, considering that the separated positions even at a low flow rate of 1 µL min^{-1} were not changed (Fig. 5b), the underlying principle of the hydrophoretic separation is the interaction between a particle and the structure-induced pressure field, not gravity.

Hydrophoretic separation

Fig. 6 shows the hydrophoretic separation of mixed particles with diameters of 9 and 12 µm. For this test, the microfluidic device with 19 µm-height obstacles was used at the applied flow rate of 1 µL min^{-1}. In the separation process, there were no physical interferences between the movements of 9 µm beads in the oscillating mode and 12 µm beads in the direct mode. Thus, the lateral position of separated particles in Fig. 6a and 6b corresponds well to the individually characterized data in Fig. 5a (supplementary video, see ESI‡). The volume fraction of the injected particles was ~0.02% (v/v). At the moderate concentration, particles can pass through a channel one by one, so that the collision between particles is negligible. 9 and 12 µm-sized beads will flow adjacent to each other at the high concentration over ~2% (v/v) by simple volumetric calculation. At this concentration, particle–particle

interaction can affect the separation resolution by deforming the pressure fields and colliding with each other. The exact operational limit of particle concentration and particle–particle interaction phenomena should be further investigated in order to optimize the separation device.

Standard curve for hydrophoretic sizing

The separation profile is linearly decreased as the diameter of particles increases. We utilized these size-dependent hydrophoretic movements of particles as the signal for particle sizing. The standard curve for hydrophoretic sizing was constructed using microparticle size standards whose diameters are known. Fig. 7a shows typical position distributions of 8, 10, and 12 µm particles obtained in the expanded outlet region. These figures were acquired in the device with 23 µm-height obstacles at a flow rate of 2 µL min^{-1}. Each distribution of the particles relates to their size. As the diameter of particles increases, their hydrophoretic movements are changed from the oscillating to the direct mode because of the alignment effect by the slanted obstacle. As mentioned before, 15 and 20 µm particles having a comparable size to the obstacles are aligned to the center of the z-axis. Therefore, they are exposed to the identical pressure field: thereby they will flow to the same lateral region, the base area (Fig. 7a). In the hydrophoretic sizing, the base area means the state when particles are fully focused to a sidewall at a given obstacle height. The base area was below the lateral position of 65.1 µm in the device with 23 µm-height obstacles (Fig. 7b). Also, when we
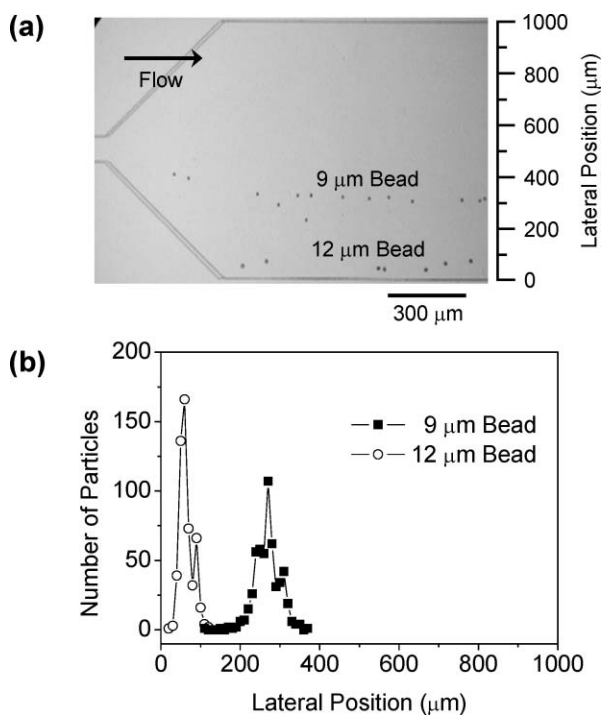

Fig. 6 (a) Optical micrograph showing separated particle positions. (b) Measured profiles of the separated particle positions. 9 and 12 µm beads were injected into the device with 19 µm-height obstacles at 1 µL min^{-1}. They were identified by size difference.
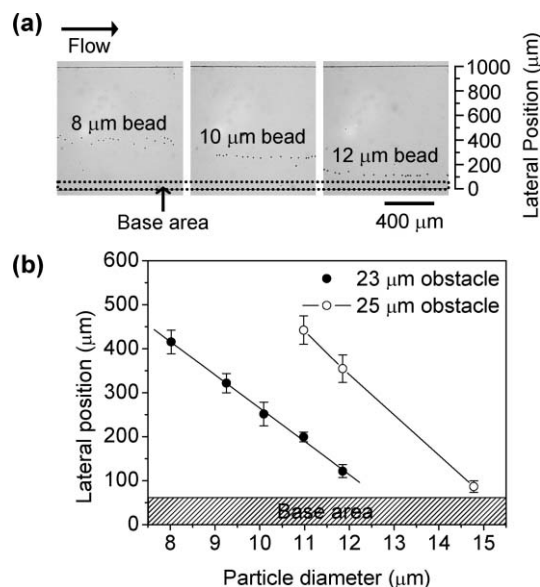

Fig. 7 Calibration of the microfluidic device for hydrophoretic sizing. (a) Optical micrographs showing position distributions of size-standard beads in the expanded outlet region of 1 mm. 8, 10, and 12 µm beads were injected into the microfluidic device with slanted obstacles of 23 µm height. (b) Lateral positions of particles as the function of their sizes. The solid line for 23 µm obstacles is a linear regression line to obtain a standard curve for particle sizing. The lines for 25 µm obstacles just connect each data point. Each error bar represents the standard deviation from the measurements of more than 100 particles.

injected 6.6 μm beads in the device, their lateral position was overlapped with those of 8 to 12 μm beads (data not shown). Accordingly, we can determine the sizing limit to be 8 μm, the smallest diameter we can size at a given obstacle height. In the sizing range of 8 to 12 μm diameter, we can plot a linear standard curve (Fig. 7b) with R^2 = 0.998. When solving the standard curve for diameter (D), we obtain,

$$D = \frac{1}{R_{P-D}}(P_i - P) \qquad (2)$$

where D is the diameter, R_{P-D} is the conversion ratio of the diameter to the lateral position, P is the lateral position in the expanded outlet region, and P_i is the position intercept when the diameter is zero. For the device with 23 μm-height obstacles, R_{P-D} and P_i were −75.6 and 1020.8, respectively.

The size difference between the gap of slanted obstacles and a particle is a modulation factor to determine the sizing range of particles. Since the hydrophoretic movement depends on the alignment effect by the slanted obstacle, we can extend the sizing range by changing the height of the obstacle. To modulate the sizing range, we carried out an additional calibration of the device with 25 μm-height obstacles. As the height of the obstacle increases from 23 to 25 μm, 12 μm beads change their hydrophoretic movements from the direct to the oscillating mode (Fig. 7b). Accordingly, the overall sizing range was shifted to the right compared to the above experiment in the device with 23 μm-height obstacles. Also, when we injected 10 μm beads in the device with 25 μm-height obstacles, their lateral position was overlapped with those of 11 to 15 μm beads. Therefore, in the device with 25 μm-height obstacles, the sizing limit was 11 μm.

Hydrophoretic sizing

The hydrophoretic sizing was performed with the above calibration curve (Fig. 7b) and compared with a conventional laser diffraction method. For the demonstration of the hydrophoretic sizing, 10.4 μm beads with a relatively high CV of 8.7% were used as a model particle. The 10.4 μm beads were injected into the microfluidic device with 23 μm-height obstacles at a flow rate of 2 μL min⁻¹. As shown in Fig. 8a, the beads were distributed according to their specific sizes in the expanded outlet region of 1 mm. The bead position was measured within 210 ± 53 μm. This position was converted into the diameter of 10.7 ± 0.7 μm by the linear calibration curve obtained from Fig. 7b (Fig. 8b). In this experiment, the feed size polydispersity (defined as the standard deviation of the particle diameter divided by the mean particle diameter) was 6.5%. The estimated diameter of the bead well agrees with the measured result from a laser diffraction particle size analyzer (LS 13 320; Beckman Coulter, Inc.), 10.4 ± 0.9 μm. Conventional particle sizing methods typically require precise physical parameters such as refractive index.[28] Also, their high laser and electric fields for measurement can damage biological samples like cells, which can cause large sizing errors. Our microfluidic sizing technique overcomes these drawbacks and can be applied to a versatile particle sizing method as an alternative.
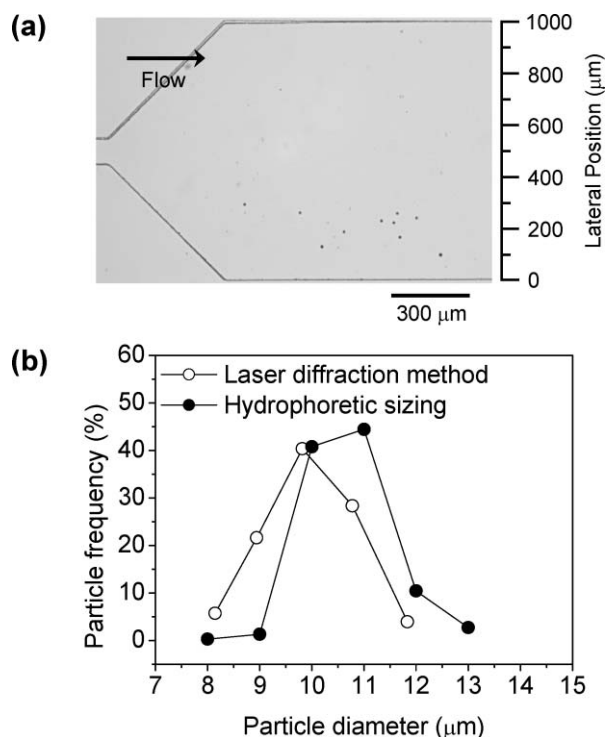

Fig. 8 Hydrophoretic sizing of 10.4 μm bead with CV of 8.7% for its diameter. (a) Optical micrographs showing the position distribution of 10.4 μm beads in the expanded outlet region of 1 mm. They were injected into the microfluidic device with slanted obstacles of 23 μm height. (b) Size distributions of 10.4 μm beads measured using the hydrophoretic method and a laser diffraction analyzer. The plot for hydrophoretic sizing was obtained from the measurement of 1071 particles.

Conclusions

In conclusion, hydrophoresis was applied to the high-resolution separation and to the sizing of microparticles without any accurate and complex detection equipment. Our experiments show the ability of hydrophoresis to discriminate microbeads with diameter differences of ∼7.3% and to separate 9 and 12 μm beads. This value for the diameter difference is lower than ∼12.6% and 30% of other passive separation methods,[22,25] although the working range is different. In our device, the size limit or operational limit means the smallest diameter able to be resolved. For the device with 23 μm-height obstacles, the limit was 8 μm in the operational range of 8 to 12 μm. To lower the limit below the sub-micron ranges, introduction of sub-micron channels and the effect of Brownian motion should be considered. In addition, the operational range was adjustable by changing the height of the slanted obstacle. As the height of the obstacle increased from 23 to 25 μm, the range was changed from 8 to 12 μm to 11 to 15 μm. Therefore, the hydrophoretic device can extend its operation range or tolerance to feed size polydispersity by introduction of the device with multiple obstacle-heights. The flow-rate independence of hydrophoresis was also described within the flow-rate range of 5 μL min⁻¹. This is an important feature in developing integrated microfluidic devices where precise flow-rate control is difficult to achieve. Due to the simple design and fabrication of the device, it can be easily

integrated with other microfluidic components such as droplet and particle generators conducting on-chip sizing and sorting.

Acknowledgements

References

1 P. Sethu, A. Sin and M. Toner, *Lab Chip*, 2006, **6**, 83.
2 D. Melucci, M. Guardigli, B. Roda, A. Zattoni, P. Reschiglian and A. Roda, *Talanta*, 2003, **60**, 303.
3 P. Reschiglian, A. Zattoni, D. Melucci, B. Roda, M. Guardigli and A. Roda, *J. Sep. Sci.*, 2003, **26**, 1417.
4 P. Reschiglian, A. Zattoni, B. Roda, E. Michelini and A. Roda, *Trends Biotechnol.*, 2005, **23**, 475.
5 J. M. Metreau, S. Gallet, P. J. P. Cardot, V. L. Maire, F. Dumas, A. Hernvann and S. Loric, *Anal. Biochem.*, 1997, **251**, 178.
6 S. Battu, A. Roux, S. Delebasee, C. Bosgiraud and Ph. J. P. Cardot, *J. Chromatogr., B: Biomed. Appl.*, 2001, **751**, 131.
7 A. Bernard, B. Paulet, V. Colin and Ph. J. P. Cardot, *Trends Anal. Chem.*, 1995, **14**, 266.
8 P. Reschiglian, A. Zattoni, B. Roda, S. Casolari, M. H. Moon, J. Lee, J. Jung, K. Rodmalm and G. Cenacchi, *Anal. Chem.*, 2002, **74**, 4895.
9 X.-B. Wang, J. Yang, Y. Huang, J. Vykoukal, F. F. Becker and P. R. C. Gascoyne, *Anal. Chem.*, 2000, **72**, 832.
10 J. Yang, Y. Huang, X.-B. Wang, F. F. Becker and P. R. C. Gascoyne, *Biophys. J.*, 2000, **78**, 2680.
11 C. B. Fuh and J. C. Giddings, *Biotechnol. Prog.*, 1995, **11**, 14.
12 L. Sun, M. Zborowski, L. R. Moore and J. J. Chalmers, *Cytometry*, 1998, **33**, 469.
13 D. J. Beebe, G. A. Mensing and G. M. Walker, *Annu. Rev. Biomed. Eng.*, 2002, **4**, 261.
14 J. El-Ali, P. K. Sorger and K. F. Jensen, *Nature*, 2006, **442**, 403.
15 X.-B. Wang, J. Vykoukal, F. F. Becker and P. R. C. Gascoyne, *Biophys. J.*, 1998, **74**, 2689.
16 S. Choi and J.-K. Park, *Lab Chip*, 2005, **5**, 1161.
17 J. G. Kralj, M. T. W. Lis, M. A. Schmidt and K. F. Jensen, *Anal. Chem.*, 2006, **78**, 5019.
18 N. Pamme and A. Manz, *Anal. Chem.*, 2004, **76**, 7250.
19 U. Seger-Sauli, M. Panayiotou, S. Schnydrig, M. Jordan and P. Renaud, *Electrophoresis*, 2005, **26**, 2239.
20 M. P. MacDonald, G. C. Spalding and K. Dholakia, *Nature*, 2003, **426**, 421.
21 I. Ricárdez-Vargas, P. Rodríguez-Montero, R. Ramos-García and K. Volke-Sepúlveda, *Appl. Phys. Lett.*, 2006, **88**, 121116.
22 L. R. Huang, E. C. Cox, R. H. Austin and J. C. Sturm, *Science*, 2004, **304**, 987.
23 M. Yamada, M. Nakashima and M. Seki, *Anal. Chem.*, 2004, **76**, 5465.
24 M. Yamada and M. Seki, *Lab Chip*, 2005, **5**, 1233.
25 M. Yamada and M. Seki, *Anal. Chem.*, 2006, **78**, 1357.
26 S. Choi and J.-K. Park, *Proc. Micro Total Analysis Systems 2006 Conference*, Tokyo, Japan, 2006, pp. 371–373.
27 A. D. Stroock, S. K. Dertinger, G. M. Whitesides and A. Ajdari, *Anal. Chem.*, 2002, **74**, 5306.
28 A. Beekman, D. Shan, A. Ali, W. Dai, S. Ward-Smith and M. Goldenberg, *Pharm. Res.*, 2005, **22**, 518.